

# Impact of Conduit Geometry on the Performance of Typical Particulate Microchip Packings

Stephanie Jung,<sup>†</sup> Alexandra Höltzel,<sup>†</sup> Steffen Ehlert,<sup>†</sup> Jose-Angel Mora,<sup>‡</sup> Karsten Kraiczek,<sup>‡</sup> Monika Dittmann,<sup>‡</sup> Gerard P. Rozing,<sup>‡</sup> and Ulrich Tallarek<sup>\*,†</sup>

Department of Chemistry, Philipps-Universität Marburg, Hans-Meerwein-Strasse, 35032 Marburg, Germany, and Agilent Technologies, Hewlett-Packard-Strasse 8, 76337 Waldbronn, Germany

This work investigates the impact of conduit geometry on the chromatographic performance of typical particulate microchip packings. For this purpose, high-performance liquid chromatography (HPLC)/UV-microchips with separation channels of quadratic, trapezoidal, or Gaussian cross section were fabricated by direct laser ablation and lamination of multiple polyimide layers and then slurry-packed with either 3 or 5  $\mu\text{m}$  spherical porous C8-silica particles under optimized packing conditions. Experimentally determined plate height curves for the empty microchannels are compared with dispersion coefficients from theoretical calculations. Packing densities and plate height curves for the various microchip packings are presented and conclusively explained. The 3  $\mu\text{m}$  packings display a high packing density irrespective of their conduit geometries, and their performance reflects the dispersion behavior of the empty channels. Dispersion in 5  $\mu\text{m}$  packings correlates with the achieved packing densities, which are limited by the number and accessibility of corners in a given conduit shape.

Recent advances in on-chip liquid chromatography include the development of fully integrated systems, which contain all fluidic components such as pumps, sample injectors, and separation columns on-chip,<sup>1–3</sup> as well as the fabrication of high-pressure rating microfluidic devices.<sup>4,5</sup> Open tubulars,<sup>6–8</sup> ordered pillar arrays,<sup>9,10</sup> polymer and silica monoliths<sup>11–18</sup> as well as slurry-

packed particulate beds<sup>19–22</sup> have all been used for chromatographic separation on microchips but, up to now, rarely with a focus on separation efficiency. The use of particulate packings offers the advantage over microfabricated support structures that all issues regarding the wide variety of desired surface chemistries for tailoring separations can be addressed externally (off-chip) on bulk stationary phase material, as done in high-performance liquid chromatography (HPLC) practice. However, slurry-packing of microchips is often carried out manually with a syringe or with pumps at low to moderate pressure, as most microchip channels, fittings, and packaging are sensitive against high pressure. But if particulate microchip packings are to achieve separation efficiencies comparable with (or even better than) those in nano-HPLC, optimized packing conditions including high packing pressures and the application of ultrasound are essential.<sup>23</sup>

Microchip packings also deviate from the packed fused-silica capillaries of nano-HPLC by their noncylindrical conduit geometry, whose influence on hydrodynamic dispersion and thus separation efficiency has to be considered. The exact cross-sectional geometry of a microchannel depends on the methods and materials used for its fabrication. Separation channels on LC-microchips have featured semicircular, quadratic, rectangular, trapezoidal, and elliptical cross sections, often with deviations from regular geometries. A systematic numerical simulations study of random

\* Corresponding author. Phone: +49-(0)6421-28-25727. Fax: +49-(0)6421-28-22124. E-mail: tallarek@staff.uni-marburg.de.

<sup>†</sup> Philipps-Universität Marburg.

<sup>‡</sup> Agilent Technologies.

- (1) Xie, J.; Miao, Y.; Shih, J.; Tai, Y.-C.; Lee, T. D. *Anal. Chem.* **2005**, *77*, 6947–6953.
- (2) Lazar, I. M.; Trisiripisal, P.; Sarvaiya, H. A. *Anal. Chem.* **2006**, *78*, 5513–5524.
- (3) Borowsky, J. F.; Giordano, B. C.; Lu, Q.; Terray, A.; Collins, G. E. *Anal. Chem.* **2008**, *80*, 8287–8292.
- (4) Liu, J.; Chen, C.-F.; Tsao, C.-W.; Chang, C.-C.; Chu, C.-C.; DeVoe, D. L. *Anal. Chem.* **2009**, *81*, 2545–2554.
- (5) Koesdjojo, M. T.; Koch, C. R.; Remcho, V. T. *Anal. Chem.* **2009**, *81*, 1652–1659.
- (6) Manz, A.; Miyahara, Y.; Miura, J.; Watanabe, Y.; Miyagi, H.; Sato, K. *Sens. Actuators, B* **1990**, *1*, 249–255.
- (7) Vahey, P. G.; Smith, S. A.; Costin, C. D.; Xia, Y. N.; Brodsky, A.; Burgess, L. W.; Synovec, R. E. *Anal. Chem.* **2002**, *74*, 177–184.
- (8) Schlund, M.; Gilbert, S. E.; Schnydrig, S.; Renaud, P. *Sens. Actuators, B* **2007**, *123*, 1133–1141.
- (9) De Malsche, W.; Eghbali, H.; Clicq, D.; Vangelooven, J.; Gardeniers, H.; Desmet, G. *Anal. Chem.* **2007**, *79*, 5915–5926.

- (10) Illa, X.; De Malsche, W.; Bomer, J.; Gardeniers, H.; Eijkel, J.; Morante, J. R.; Romano-Rodriguez, A.; Desmet, G. *Lab Chip* **2009**, *9*, 1511–1516.
- (11) Reichmuth, D. S.; Shepodd, T. J.; Kirby, B. J. *Anal. Chem.* **2005**, *77*, 2997–3000.
- (12) Ro, K. W.; Liu, J.; Knapp, D. R. *J. Chromatogr., A* **2006**, *1111*, 40–47.
- (13) Carlier, J.; Arscott, S.; Thomy, V.; Camart, J. C.; Cren-Olivé, C.; Le Gac, S. *J. Chromatogr., A* **2005**, *1071*, 213–222.
- (14) Yang, Y.; Li, C.; Kameoka, J.; Lee, K. H.; Craighead, H. G. *Lab Chip* **2005**, *5*, 869–876.
- (15) Mair, D. A.; Geiger, E.; Pisano, A. P.; Fréchet, J. M. J.; Svec, F. *Lab Chip* **2006**, *6*, 1346–1354.
- (16) Ishida, A.; Yoshikawa, T.; Natsume, M.; Kamidate, T. *J. Chromatogr., A* **2006**, *1132*, 90–98.
- (17) Liu, J.; Ro, K. W.; Nayak, R.; Knapp, D. R. *Int. J. Mass Spectrom.* **2007**, *259*, 65–72.
- (18) Levkin, P. A.; Eelink, S.; Stratton, T. R.; Brennen, R.; Robotti, K.; Yin, H.; Killeen, K.; Svec, F.; Fréchet, J. M. J. *J. Chromatogr., A* **2008**, *1200*, 55–61.
- (19) Yin, H.; Killeen, K.; Brennen, R.; Sobek, D.; Werlich, M.; van de Goor, T. *Anal. Chem.* **2005**, *77*, 527–533.
- (20) Shih, C.-Y.; Chen, Y.; Xie, J.; He, Q.; Tai, Y.-C. *J. Chromatogr., A* **2006**, *1111*, 272–278.
- (21) Gaspar, A.; Piyasena, M. E.; Gomez, F. A. *Anal. Chem.* **2007**, *79*, 7906–7909.
- (22) Yang, Y.; Chae, J. *Appl. Phys. Lett.* **2009**, *94*, 173902.
- (23) Ehlert, S.; Kraiczek, K.; Mora, J.-A.; Dittmann, M.; Rozing, G. P.; Tallarek, U. *Anal. Chem.* **2008**, *80*, 5945–5950.

sphere packings in conduits with circular, quadratic, rectangular, and semicircular cross section revealed increased axial dispersion with increasing deviation from cylindrical conduit symmetry.<sup>24</sup> Additionally, the corner regions of noncylindrical conduits are more difficult to pack densely. In trapezoidal conduits, a large ratio between the two base lengths and the deviation from orthogonality of the base corners increase dispersion.<sup>25</sup> The effects that lead to increased dispersion depend strongly on the packing density. In densely packed beds, the effects of the specific conduit geometry become small and band broadening approaches that of comparable cylindrical packings.<sup>24</sup>

A third aspect that influences packing structure and thus separation efficiency is the low particle-aspect (conduit-to-particle size) ratio of particulate microchip packings.<sup>26</sup> This aspect is also relevant in nano-HPLC as the reduction of channel or capillary dimensions with respect to conventional HPLC columns is not accompanied by a corresponding reduction in mean particle size.<sup>27–30</sup> The geometrical wall effect results from the inability of the particles to form a close packing against the conduit walls. The particle layer closest to the conduit wall is highly ordered and differs significantly from subsequent layers, because the interstitial space between wall and first particle layer cannot be partially occupied by other particles. In subsequent layers toward the center the order decreases until the arrangement of the particles becomes random.<sup>31</sup> At low particle-aspect ratios, the highly ordered wall region—which can cover a distance of 4–5 particle diameters for spherical monodisperse particles—constitutes a large fraction of the conduit volume, and the mean interparticle porosity of the packing increases.<sup>26,30,31</sup>

Although the merits of numerical simulation methods are unquestionably the systematic study of isolated parameters like conduit geometry, conduit dimensions, particle-aspect ratio, or packing density, with high precision and detail, experimental studies of microchip packings are a necessary complement as they represent real-life conditions and applications.<sup>32</sup> For example, the decision to use a certain separation channel geometry on a microchip is not only a design option informed by considerations about hydrodynamic dispersion but also a fabrication issue as certain geometries are more or less elaborate or even impossible to realize with a chosen method.

Our current work is an experimental study of axial dispersion in particulate microchip packings contained in channels of different cross-sectional geometries. We use polyimide HPLC/UV-microchips that integrate sample injection, separation, and UV detection (Figure 1). Microchips containing separation channels with trapezoidal, quadratic, or Gaussian cross section were fabricated by direct laser ablation and lamination of multiple polyimide layers

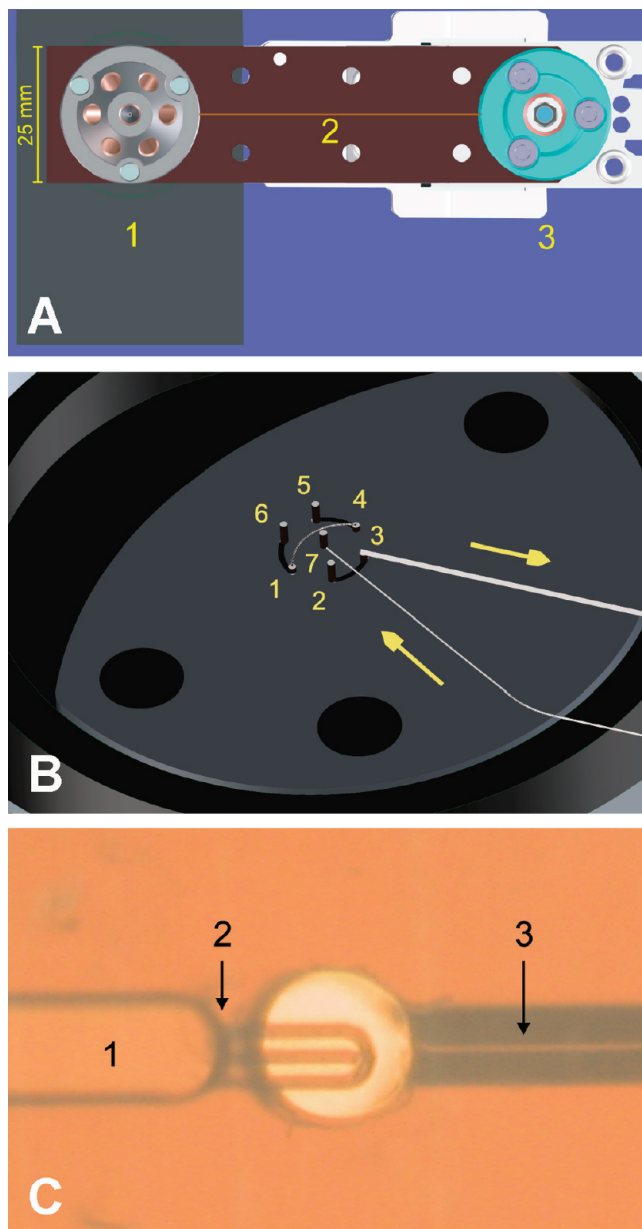


**Figure 1.** (A) Microchip sandwiched between the stator and rotor of a Rheodyne injection valve (1), providing dead-volume-free injection onto the separation channel (2) and on-chip UV detection with a special holder (3). (B) The injection unit of the microchips consists of seven ports with an internal sample loop between ports 1 and 4. The sample is injected onto the separation channel at port 3 and redirected after passing the detection cell via port 7 to an external flow sensor. (C) A micromachined outlet frit (2) is used to retain the packing material at the end of the separation channel (1). A narrow channel (3) provides the connection between outlet frit and detection cell.

(Figure 2). Due to the Gaussian-shaped energy profile of the laser, Gaussian cross sections are straightforward to realize with this fabrication method, whereas quadratic cross sections require the most effort. The investigated microchips represent typical real-life examples where deviations from regular cross-sectional geometries and small variations in channel dimensions are the inevitable result of the fabrication process. Microchips were slurry-packed with spherical porous C8-modified silica particles of either 3 or 5  $\mu\text{m}$  nominal particle size. Both packing materials have the same surface chemistry as well as very similar particle size

(24) Khirevich, S.; Hölzel, A.; Hlushkou, D.; Tallarek, U. *Anal. Chem.* **2007**, *79*, 9340–9349.

(25) Khirevich, S.; Hölzel, A.; Hlushkou, D.; Seidel-Morgenstern, A.; Tallarek, U. *Lab Chip* **2008**, *8*, 1801–1808.

(26) Jung, S.; Ehlert, S.; Mora, J.-A.; Kraiczek, K.; Dittmann, M.; Rozing, G. P.; Tallarek, U. *J. Chromatogr., A* **2009**, *1216*, 264–273.

(27) Kennedy, R. T.; Jorgenson, J. W. *Anal. Chem.* **1989**, *61*, 1128–1135.

(28) Hsieh, S.; Jorgenson, J. W. *Anal. Chem.* **1996**, *68*, 1212–1217.

(29) Patel, K. D.; Jerkovich, A. D.; Link, J. C.; Jorgenson, J. W. *Anal. Chem.* **2004**, *76*, 5777–5786.

(30) Ehlert, S.; Rösler, T.; Tallarek, U. *J. Sep. Sci.* **2008**, *31*, 1719–1728.

(31) de Klerk, A. *AIChE J.* **2003**, *49*, 2022–2029.

(32) Khirevich, S.; Hölzel, A.; Ehlert, S.; Seidel-Morgenstern, A.; Tallarek, U. *Anal. Chem.* **2009**, *81*, 4937–4945.

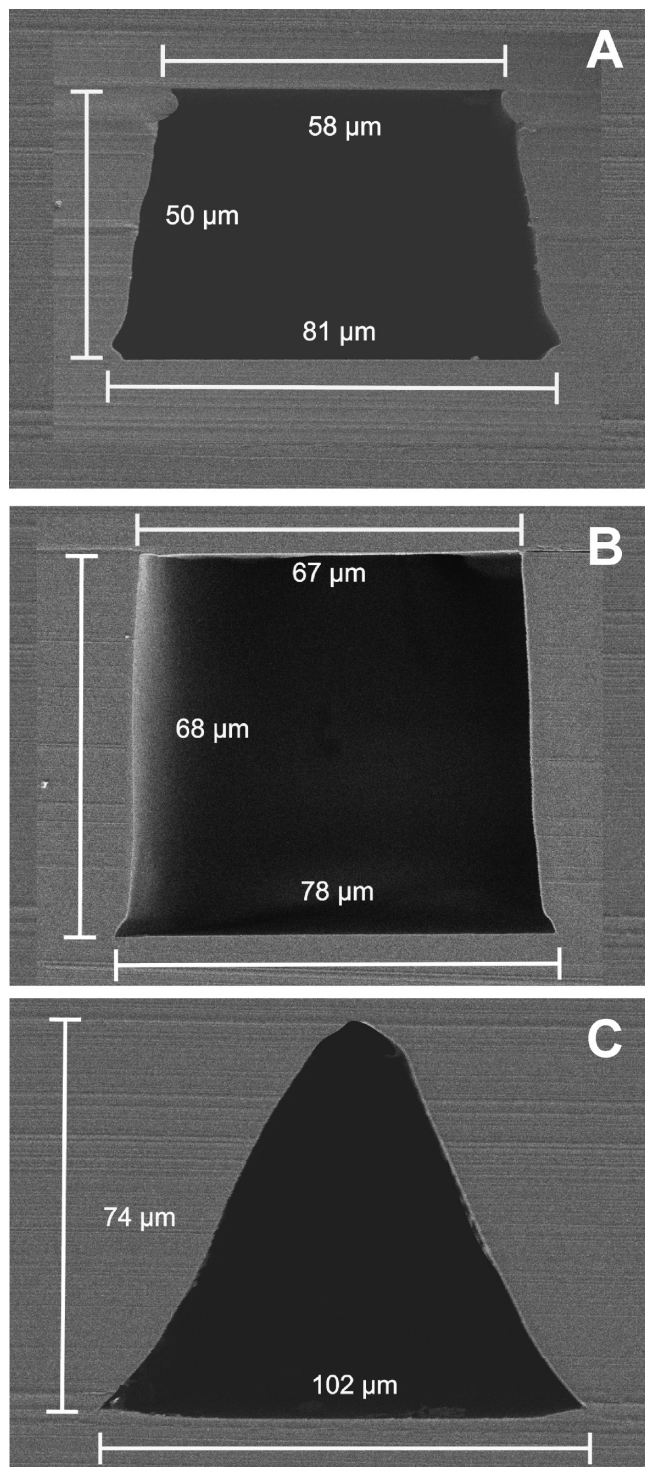


**Figure 2.** SEM images (equal scaling) of empty microchip separation channels with trapezoidal (A), pseudoquadratic (B), and Gaussian (C) cross sections. Unpacked microchips were cut vertically through their separation channels. The gap visible in the upper right corner of the pseudoquadratic channel (B) is an artifact from the cutting process.

distributions, mean intraparticle pore sizes and porosities,<sup>26</sup> enabling us to study the influence of the particle-aspect ratio on the performance of the microchip packings.

## EXPERIMENTAL SECTION

**Chemicals and Materials.** HPLC grade organic solvents (acetonitrile, methylene chloride, methanol, and acetone) and

analytes (uracil, benzene, ethylbenzene, *n*-propylbenzene, *n*-butylbenzene, and *n*-pentylbenzene) were purchased from Sigma-Aldrich Chemie GmbH (Taufkirchen, Germany). HPLC grade water was prepared using a Milli-Q gradient water purification system (Millipore, Bedford, MA). Polystyrene standard (100 000 g mol<sup>-1</sup>) was purchased from Fluka Chemie GmbH (Buchs, Switzerland). Chromatographic packing materials Hypersil MOS (monomeric octyl silica, C8) of 3 and 5 μm nominal particle diameter were bought from Thermo Fisher Scientific Inc. (Waltham, MA). Both packing materials have a mean intraparticle pore diameter of 126–142 Å, a surface area of 165–180 m<sup>2</sup> g<sup>-1</sup>, and an intraparticle porosity of  $\epsilon_{\text{intra}} \sim 0.4$ .<sup>26</sup>

**Microchip Fabrication.** The fabrication process consists of UV laser ablation of polyimide foils to form microfluidic channels and ports, followed by a cleaning step to remove residues from laser ablation; the polyimide films are then precisely aligned before vacuum lamination under heat and pressure.<sup>19</sup> Two types of polyimide foils are used in the fabrication: (1) 50 μm thick bonding foils, which have a coextruded thermoplastic polyimide adhesive layer on each side that bonds to polyimide when heat and pressure are applied, and (2) 75 or 125 μm thick foils without adhesive layer (nonadhesive foils), which confine the microchips at the exterior. Different cross-sectional geometries for the separation channels were realized by varying the thickness and number of the polyimide layers and the parameters of direct laser ablation. Microchips with trapezoidal separation channel consist of three polyimide layers: a central bonding layer (50 μm) out of which the channel features were laser-cut, and nonadhesive top and bottom layers of 125 μm thickness each. Microchips with quadratic and Gaussian channel cross sections are based on a five-layer design, in which a central (nonadhesive) foil is enveloped by two bonding inner foils (50 μm each) and two nonadhesive outer foils (125 μm each) that prevent the microchips from sticking to the lamination device. Microchips with a quadratic separation channel have a central layer of 75 μm thickness out of which the channel features were laser-cut. For microchips with a Gaussian separation channel, the spatial energy distribution of the laser was used to cut a Gaussian profile into the central layer of 125 μm thickness. The separation channels on each microchip have a total length of 73 mm and a micromachined outlet frit at the end to retain the packing. Microchips showing signs of channel deformation, polyimide damage, or other aberrations (e.g., large channel volumes indicating leakage) were discarded.

For sample injection the microchips were attached to a face-seal rotary valve (Figure 1A) with a 0.7 nL internal loop between ports 1 and 4 (Figure 1B). Each port contributes another 2.2 nL to the sample volume. The sample is injected dead-volume-free onto the packed bed inside the separation channel (port 3, Figure 1B). A prototype UV detection cell of 50 μm i.d. was installed behind the outlet frit. The path length of the cell equals the overall thickness of the respective microchips (i.e., 300 μm for trapezoidal, 425 μm for quadratic, and 475 μm for Gaussian cross sections). The detection cell was connected to a diode-array UV detector with a special holder. The resulting dead volume between outlet frit and detection cell for the microchips (Figure 1C) varied between 2.5 and 3 nL, depending on number and thickness of the polyimide layers. In comparison with the volume of the empty

**Table 1. Dispersion in the Empty Microchannels**

cross-sectional geometry	channel volume $V_{\text{ch}}^a$	narrower transverse length $h$ in eq 2 <sup>b,c</sup>	shape function $f$ in eq 2 <sup>b,d</sup>	
			range <sup>d</sup>	mean <sup>d</sup>
trapezoidal	265 ± 8.8 nL	50 μm (height)	2.2–2.7	2.4
quadratic	424 ± 8.1 nL	68 μm (height)	1.9–2.3	2.2
		54 μm (fwhm)	2.6–3.2	2.8
Gaussian	291 ± 2.4 nL	74 μm (height)	1.4–1.7	1.5
		51 μm (half the bottom length)	2.8–3.5	3.1

<sup>a</sup> Channel volumes were experimentally determined and represent the average of 10 individual microchips with the indicated channel geometry. <sup>b</sup> Ref 35. <sup>c</sup> Values were taken from the SEM cuts of individual microchips (Figure 2). <sup>d</sup> Values were calculated from the normalized plate height curves of 10 individual microchips with the indicated channel geometry.

separation channels (Table 1), the dead volume from sample injection and detection is negligibly small.

**Microchip Packing.** Slurry liquids were prepared by suspending 50 mg of dry particles in 1 mL of acetone. Methanol was used as pushing solvent in the packing process.<sup>33</sup> The microchips were tightly fixed into a custom-built stainless steel holder to avoid damage to the polyimide foils during the application of high packing pressures and ultrasonication and connected to the packing station via port 3 (Figure 1B). The packing station consists of a WellChrom K-1900 pneumatic pump (Knauer GmbH, Berlin, Germany) connected by an SSI three-way valve (ERC, Riemerling, Germany) to a 500 μm i.d. glass-lined metal tubing used as slurry reservoir. After filling the slurry reservoir the microchips were inserted into an ultrasonic bath and the packing procedure started by applying 300 bar pressure and ultrasound for 15 min. Then, the ultrasonic bath was switched off and the system slowly depressurized for at least 20 min. Afterward, microchips were inspected microscopically for damages along the separation channel and gaps inside the packing. For quadratic and Gaussian channels, two microchips of each geometry were packed with 3 μm particles and two with 5 μm particles. Three microchips with trapezoidal channels were packed with 3 μm particles and three with 5 μm particles.

**Chromatographic Measurements.** All data were acquired with an Agilent 1100 liquid chromatograph consisting of a degasser, a nanopump, and a diode-array UV detector. Volumetric flow rates were continuously monitored by an external flow sensor (model SLG-1430-150, Sensirion, Stäfa, Switzerland) connected to the analytical system via port 7 (Figure 1B) to which the mobile phase was redirected after passing the detection cell to determine actual pump errors and identify possible leakage immediately. The chromatograph was operated with Agilent ChemStation software (rev. B.02.01-SR1). All experiments were carried out at 298 ± 1 K under isocratic elution conditions. Injections were repeated three times for a given microchip and flow rate, and the results were averaged to account for the error from manual injection.

Channel volumes  $V_{\text{ch}}$  and plate height curves of the empty microchips were determined by injection of 0.66 mM *n*-pentylbenzene dissolved in the mobile phase of acetonitrile/water 70/30 (v/v) and detection at 210 nm. Ten individual microchips of each channel geometry were investigated, and the results were averaged to account for slight variations in channel dimensions (Table 1).

Porosities of the packed microchips were analyzed by inverse size exclusion chromatography.<sup>26,30</sup> A sample of 1 mM benzene (a small, nonretained analyte with access to the total pore volume of the packing,  $V_{\text{total}}$ ) and 0.66 mM polystyrene standard (100 000 g mol<sup>-1</sup>, completely size-excluded from the intraparticle pore space) dissolved in the mobile phase of methylene chloride was injected and chromatographed at a flow rate of 300 nL min<sup>-1</sup> and detection at 230 nm. Total bed porosities ( $\epsilon_{\text{total}}$ ) were derived from  $\epsilon_{\text{total}} = V_{\text{total}}/V_{\text{ch}}$ , and interparticle porosities ( $\epsilon_{\text{inter}}$ ) from  $\epsilon_{\text{inter}} = V_{\text{inter}}/V_{\text{ch}}$ , where  $V_{\text{inter}}$  is the interparticle void volume of the microchip packings determined from the elution volume of the polystyrene standard. Finally, intraparticle porosities ( $\epsilon_{\text{intra}}$ ) were calculated from the relation  $\epsilon_{\text{total}} = \epsilon_{\text{inter}} + (1 - \epsilon_{\text{inter}})\epsilon_{\text{intra}}$ .

Plate height curves of the packed microchips were determined with acetonitrile/water 70/30 (v/v) as mobile phase and detection at 210 nm. The sample consisted of 0.33 mM uracil, 0.66 mM benzene, and 0.66 mM of each alkylbenzene dissolved in the mobile phase. Plate heights were calculated using the Agilent ChemStation software based on a pseudomethod of moments.

## RESULTS AND DISCUSSION

In Figure 2 scanning electron microscopy (SEM) images of vertical cuts through the unpacked microchip separation channels visualize each of the investigated cross-sectional geometries. Trapezoidal and quadratic channels were fabricated by cutting a hole of the required width and length (73 mm) into a polyimide foil of the necessary thickness and then laminating the cut-out foil to the enveloping polyimide layers. Accordingly, the side walls of trapezoidal and quadratic channels originate from the central polyimide foil, whereas top and bottom walls are formed by the enveloping polyimide layers. The trapezoidal cross section (Figure 2A) has a height of 50 μm, a top base of 58 μm, a bottom base of 81 μm, and a base angle of ca. 80°. The four corners are irregular and each of a different shape, a result of the spatial energy profile of the laser, laser defocusing effects, and the lamination process. The cross section of the quadratic channel (Figure 2B) is in fact trapezoidal. The top corners are nearly rectangular, but the bottom corners are peaked, and the base lengths are unequal with 67 μm at the top and 78 μm at the bottom. A truly quadratic channel turned out too difficult to fabricate, as particularly the effects of the lamination process on the final cross-sectional shape cannot be directed precisely. For example, the height of the quadratic channel that was expected to equal the thickness of the central polyimide foil (75 μm) is only 68 μm. For fabrication of the Gaussian channel, the Gaussian spatial energy profile of the laser

(33) Vissers, J. P. C.; Claessens, H. A.; Laven, J.; Cramers, C. A. *Anal. Chem.* 1995, 67, 2103–2109.

was used to carve the channel profile into a polyimide layer of sufficient thickness. The side walls and the top originate from the central layer, whereas the bottom wall is formed by one of the enveloping layers. The Gaussian cross section (Figure 2C) has a bottom length (from corner to corner) of 102  $\mu\text{m}$ , a height of 74  $\mu\text{m}$ , and a fwhm (full width at half-maximum) of 54  $\mu\text{m}$ . The channel base is bordered by two corners with a ca. 45° opening.

**Dispersion in the Empty Separation Channels.** The influence of the conduit geometry on flow and dispersion in open microchannels has been extensively studied, mostly by numerical analysis methods.<sup>34–40</sup> Axial dispersion of a tracer pulse injected into a fluid in laminar flow through a conduit is caused by the interaction of lateral diffusion and the nonuniform flow profile. Taylor<sup>41</sup> and Aris<sup>42</sup> have shown that axial dispersion of the solute leads to a Gaussian area-average concentration profile sufficiently far downstream (long-time limit). Dispersion in cylindrical conduits can then be described by<sup>43</sup>

$$\frac{D_{\text{ax}}}{D_{\text{m}}} = 1 + \frac{1}{192} \left( \frac{ud}{D_{\text{m}}} \right)^2 = 1 + \frac{1}{192} Pe^2 \quad (1)$$

where  $D_{\text{ax}}$  is the axial dispersion coefficient,  $D_{\text{m}}$  is the molecular diffusion coefficient,  $u$  is the flow velocity averaged over the cross section,  $d$  is the cylinder diameter, and  $Pe = ud/D_{\text{m}}$  the Péclet number, which gives the ratio of convective to diffusive transport rates.

A general expression to describe dispersion in noncylindrical channels was introduced by Dutta et al.<sup>35</sup> based on pressure-driven laminar flow between two parallel plates

$$\frac{D_{\text{ax}}}{D_{\text{m}}} = 1 + \frac{1}{210} f \left( \frac{uh}{D_{\text{m}}} \right)^2 = 1 + \frac{1}{210} f Pe^2 \quad (2)$$

where  $h$  is the characteristic narrower transverse dimension of the channel (e.g., the distance between two parallel plates) and  $f$  is a shape function that quantifies dispersion based on the actual velocity profile in the channel and depends on its exact cross-sectional geometry and dimensions ( $f = 1$  for the parallel-plate geometry).  $f$  values have been calculated for various microchannel cross sections, including rectangular and trapezoidal geometries, but not Gaussian profiles.

The axial dispersion coefficient  $D_{\text{ax}}$  (usually discussed in the engineering literature) in eqs 1 and 2 can be substituted with the chromatographic axial plate height  $H$  through the relation  $D_{\text{ax}} = Hu/2$  to give the normalized plate height equations  $H/d$  or  $H/h$  versus  $Pe = ud/D_{\text{m}}$  or  $Pe = uh/D_{\text{m}}$ , respectively, for dispersion of an unretained solute in open cylindrical channels

$$\frac{H}{d} = \frac{2}{Pe} + \frac{1}{96} Pe \quad (3)$$

or in open noncylindrical channels

$$\frac{H}{h} = \frac{2}{Pe} + \frac{1}{105} f Pe \quad (4)$$

The first term in eqs 3 and 4 refers to the contribution of axial molecular diffusion to band broadening, and the second term describes the contribution from mass transfer resistance. In the investigated range of velocities the first term is negligible.

Experimental plate height data were acquired for 10 individual microchips of each channel geometry with the unretained analyte *n*-pentylbenzene and acetonitrile/water 70/30 (v/v) as mobile phase. Figure 3A shows the resulting plate height data for the three channel geometries, averaged over the results from the individual microchips, as well as data calculated with eq 3 for cylindrical conduits. Good reproducibility of experimental data was observed with a ca. 5% variation in plate heights at 1% variation in average flow velocity. The respective regression lines have

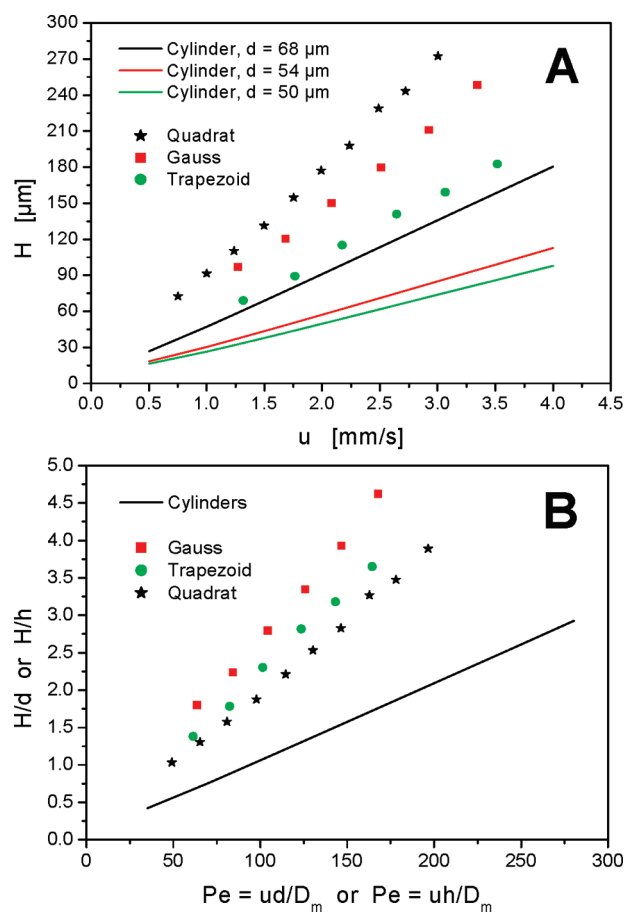


**Figure 3.** (A) Plate height curves for empty separation channels with trapezoidal (green circles), quadratic (black stars), Gaussian (red squares), and circular (solid lines) cross sections. Experimental plate height data represent the average of 10 individual microchips of a given channel geometry. Values for cylindrical channels whose diameters  $d$  correspond to the narrower transverse length  $h$  of the noncylindrical channels were calculated from eq 3. (B) Experimental and calculated plate height data  $H$  normalized by the respective narrower transverse length  $h$  of the channels or the cylinder diameter  $d$ , respectively, vs the Péclet number.

(34) Poppe, H. J. *Chromatogr., A* **2002**, *948*, 3–17.

(35) Dutta, D.; Ramachandran, A.; Leighton, D. T. *Microfluid. Nanofluid.* **2006**, *2*, 275–290.

(36) Ajdari, A.; Bontoux, N.; Stone, H. A. *Anal. Chem.* **2006**, *78*, 387–392.

(37) Bontoux, N.; Pépin, A.; Chen, Y.; Ajdari, A.; Stone, H. A. *Lab Chip* **2006**, *6*, 930–935.

(38) Zholkovskij, E. K.; Maslyah, J. H. *Chem. Eng. Sci.* **2006**, *61*, 4155–4164.

(39) Eghbali, H.; Desmet, G. J. *Sep. Sci.* **2007**, *30*, 1377–1397.

(40) Bahrami, M.; Yovanovich, M. M.; Culham, J. R. *Int. J. Heat Mass Transfer* **2007**, *50*, 2492–2502.

(41) Taylor, G. *Proc. R. Soc. London, Ser. A* **1953**, *219*, 186–203.

(42) Aris, R. *Proc. R. Soc. London, Ser. A* **1956**, *235*, 67–77.

(43) Deen, W. M. *Analysis of Transport Phenomena*; Oxford University Press: New York, 1998.

correlation coefficients of  $R^2 > 0.996$ , which is fairly good for manual injection onto a short separation column. The diameters of the cylindrical conduits were chosen to match the respective narrower transverse length of the microchip channels, i.e., the height of the trapezoidal (50  $\mu\text{m}$ ) and quadratic (68  $\mu\text{m}$ ) channels. For the Gaussian channel the fwhm (54  $\mu\text{m}$ ) was taken as a first approximation. The general trend visible in the plate height curves of Figure 3A is expected: dispersion increases with increasing channel diameter  $d$  (eq 1) or respective narrower transverse length  $h$  (eq 2), and dispersion in the empty noncylindrical microchannels is always larger than in the cylindrical conduits due to the influence of the confining walls on the flow profile.

For better comparison plate height data were normalized by the cylinder diameter ( $d$ ) or the respective narrower transverse length ( $h$ ) of the microchannels. The molecular diffusion coefficient of *n*-pentylbenzene in the mobile phase was taken from Li and Carr<sup>44</sup> as  $D_m = 1.07 \times 10^{-9} \text{ m}^2 \text{ s}^{-1}$ . The normalized data  $H/d$  or  $H/h$  versus  $Pe = ud/D_m$  or  $Pe = uh/D_m$  in Figure 3B show a change in the relative order of the dispersion curves for the noncylindrical channels. The quadratic channel has the lowest normalized plate height curve ( $H/h$ ) followed by the trapezoidal and the Gaussian channels. This finding is explicable from the symmetry of the respective channel cross sections.<sup>24</sup> The quadratic cross section has the highest symmetry, resulting in a more symmetrical flow profile and a smaller flow maldistribution term. Flow maldistribution increases with decreasing symmetry due to the growing distance between different velocities over which exchange of solute molecules needs to occur by lateral diffusion to approach asymptotic dispersion in the long-time limit. Thus, the velocity inequality of the flow pattern intrinsic to a particular conduit geometry increases with decreasing symmetry of the conduit.<sup>24</sup> Although the quadratic channel has a trapezoidal rather than quadratic cross section as shown in Figure 2B, the differences in side lengths are small enough to provide a more homogeneous flow profile and smaller axial dispersion than in the trapezoidal channel. The Gaussian cross section has one symmetry axis, but the continuous decrease in lateral diffusion length from bottom to top translates to larger friction forces in the upper part of the channel and more pronounced velocity differences between top and bottom part.

Experimental  $f$  values for the empty separation channels were derived by setting the slopes of the normalized plate height curves (determined by linear regression) equal to the mass transfer coefficient  $f/105$  of eq 4. Results are summarized in Table 1. The narrow range of the experimental  $f$  values reflects the good reproducibility of the cross-sectional geometry in microchip fabrication, as deviations in geometry would strongly affect empty channel dispersion. In a rectangular channel the velocity slow-down in the vertical side regions causes a substantial increase in the magnitude of  $f$  that grows with the ratio of channel width ( $w$ ) to channel height ( $h$ ), from  $f = 1.76$  for a quadratic cross section ( $w/h = 1$ ) to a limiting value of  $f = 7.95$  for rectangular cross section where  $w/h \rightarrow 0$ .<sup>35</sup> For microchips with quadratic channels the mean experimental value of  $f = 2.2$  is higher than the theoretical value of  $f = 1.76$ ,<sup>35</sup> reflecting the deviations of the channel cross section from regular quadratic geometry, i.e.,

unequal base lengths, a ratio of the mean width ( $w = 72.5 \mu\text{m}$ ) to height (68  $\mu\text{m}$ ) of  $w/h = 0.87$ , and the deviation from orthogonality of the bottom corners. Microchips with trapezoidal channels show a similar upward deviation from theoretical values. In trapezoidal channels the scaling of additional dispersivity quantified by  $f$  increases with the ratio of smaller base length ( $w_s$ ) to height ( $h$ ) of the channel and with increasing deviation of the base angle from orthogonality. According to Dutta et al.<sup>35</sup> a conduit with an isosceles trapezoidal cross section, a base angle of  $80^\circ$ , and a ratio of  $w_s/h = 1.0$  would give a value of  $f \approx 2$  (cf. Figure 6 in ref 35). The SEM image of the trapezoidal channel cross section in Figure 2A reveals a ratio of  $w_s/h = 1.2$ , but this would increase  $f$  only slightly. The main reason for the increased experimental value of  $f = 2.4$  is the four different irregularly angled corners in the trapezoidal channel that reduce the symmetry of the cross section and cause additional velocity slow-down in the corner regions.<sup>32</sup>

In the Gaussian channel the narrower transverse length is not straightforward to define; therefore, the channel height (74  $\mu\text{m}$ ) and half the bottom length (51  $\mu\text{m}$ ) were evaluated besides the fwhm (54  $\mu\text{m}$ ) for calculation of  $f$ . Choosing the channel height underestimates dispersion, because the resulting  $f$  values are smaller than those of the quadratic channel (Table 1). The choice of fwhm and half the bottom length as narrower transverse dimension give reasonable results. Although the so-calculated  $f$  values approach those of the trapezoidal channel, they are still larger, reflecting the velocity slow-down caused by the Gaussian channel's tapering profile. Considering that the exact channel dimensions vary between individual microchips due to the fabrication process (Table 1), both parameters are suitable for a first approximation of dispersion behavior in the Gaussian channel.

**Microchip Packing Densities.** Interparticle porosities of the microchip packings were determined by inverse size exclusion chromatography using a polystyrene standard with a molecular weight of 100 000  $\text{g mol}^{-1}$ . This standard had been identified in previous experiments for both packing materials as a suitable probe for the interparticle void space.<sup>26</sup> Total and interparticle porosities ( $\epsilon_{\text{total}}$  and  $\epsilon_{\text{inter}}$ ) were calculated from the elution volumes of benzene and the polystyrene standard, respectively, measured in one chromatographic run. Results are summarized in Table 2 and demonstrate that the achieved packing densities depend essentially on the particle size of the packing material. All 3  $\mu\text{m}$  packings display the low interparticle porosities ( $\epsilon_{\text{inter}} \approx 0.38$ ) characteristic of random-close packings, which proves that optimized packing conditions enable dense packings even in difficult conduit geometries. The interparticle porosities of the 5  $\mu\text{m}$  packings are only moderate ( $\epsilon_{\text{inter}} \approx 0.41$ ), reflecting looser packings. As the intraparticle porosities are practically identical for both packing materials ( $\epsilon_{\text{intra}} \approx 0.40$ ), the total porosities of the 3  $\mu\text{m}$  packings are also lower (Table 2).

The particle-aspect (conduit-to-particle size) ratio of confined packings is often the cause for systematic differences in packing density: at low particle-aspect ratios, a combination of the geometrical wall effect and particle characteristics, like surface roughness, size distribution, and shape, leads to a decreased packing density.<sup>31</sup> For example, for cylindrical fused-silica capillaries with inner diameters  $d$  between 30 and 250  $\mu\text{m}$  that were slurry-packed with 5  $\mu\text{m}$  porous C18-silica particles ( $d_p = 5.5$

(44) Li, J.; Carr, P. W. *Anal. Chem.* **1997**, *69*, 2530–2536.

**Table 2. Porosities of the Microchip Packings**

nominal particle size	conduit geometry	particle-aspect ratio <sup>a</sup>	$\epsilon_{\text{total}}^b$	$\epsilon_{\text{inter}}^b$	$\epsilon_{\text{intra}}$
3 $\mu\text{m}$	trapezoidal	17	0.633 $\pm$ 0.001	0.383 $\pm$ 0.002	0.405 $\pm$ 0.002
	quadratic	23	0.630 $\pm$ 0.005	0.383 $\pm$ 0.003	0.399 $\pm$ 0.006
	Gaussian	18	0.633 $\pm$ 0.002	0.379 $\pm$ 0.004	0.409 $\pm$ 0.005
5 $\mu\text{m}$	trapezoidal	10	0.643 $\pm$ 0.001	0.405 $\pm$ 0.004	0.400 $\pm$ 0.004
	quadratic	14	0.654 $\pm$ 0.002	0.423 $\pm$ 0.012	0.400 $\pm$ 0.012
	Gaussian	11	0.641 $\pm$ 0.006	0.397 $\pm$ 0.004	0.405 $\pm$ 0.007

<sup>a</sup> Particle-aspect ratios were calculated from the nominal particle size and the narrower transverse dimension of the channel cross sections (Table 1). For Gaussian channels, the fwhm was used. <sup>b</sup> Interparticle and total porosities were determined for two (quadratic, Gaussian) or three (trapezoidal) individual packings of a given type (conduit geometry, particle size). No statistical variance was found between individual packings of a given type. The rmsd values refer to thrice-repeated experiments with an individual microchip and reflect the error from manual injection.

$\mu\text{m}$ ), densely packed beds with  $\epsilon_{\text{inter}} = 0.36\text{--}0.37$  could be achieved at large particle-aspect ratios ( $d/d_p > 35$ ), whereas at decreasing particle-aspect ratio an exponential increase in the interparticle porosity was observed up to  $\epsilon_{\text{inter}} = 0.46$  at  $d/d_p \approx 5.5$ .<sup>30</sup> Considering that the particle size distributions of the packing materials used in our study are very similar to each other<sup>26</sup> and also to the packing material used in the related study with fused-silica capillaries,<sup>30</sup> the observed increase of interparticle porosities from  $\epsilon_{\text{inter}} = 0.38$  for the 3  $\mu\text{m}$  packings to  $\epsilon_{\text{inter}} \approx 0.41$  for the 5  $\mu\text{m}$  packings can be explained accordingly by the concomitant decrease of the particle-aspect ratios (Table 2). It is not straightforward to decide which dimension should be used to calculate the particle-aspect ratio for noncylindrical conduits whose cross-sectional geometries are defined by more than one parameter. We calculated particle-aspect ratios based on the identified narrower transverse dimensions of the microchannels (Table 1), but the so-derived particle-aspect ratios are tentative rather than strict values for the Gaussian and trapezoidal channels.

For the 5  $\mu\text{m}$  packings a slight increase in interparticle porosity from  $\epsilon_{\text{inter}} = 0.397$  for the Gaussian via  $\epsilon_{\text{inter}} = 0.405$  for the trapezoidal to  $\epsilon_{\text{inter}} = 0.423$  for the quadratic channels can be perceived. This is most likely related to the quantity and shape of the corners in the different channels. The Gaussian cross section has only two bottom corners with angles  $\leq 45^\circ$ , whereas the top of the channel is curved with a plateau width of  $\sim 10 \mu\text{m}$ . Thus, there is little steric hindrance for the particles to access the top part of the channel; only the two base corners are expected to be partially unoccupied. The smaller bottom corners of the trapezoidal cross section are expected to be more difficult to pack than the top corners with angles  $> 90^\circ$ . The SEM image of the empty channel cross section (Figure 2A) reveals that the trapezoidal channel corners are “softened”, probably from a creeping of glue inside the corners during the lamination step. These corners are better accessible to particles so that  $\epsilon_{\text{inter}}$  of the microchip packings in the trapezoidal channels is lower than in the quadratic channels, which contain four sharp corners.

**Separation Efficiencies.** Analysis of axial dispersion in the microchip packings was based on the isocratic separation of benzene and four alkylbenzenes, with uracil as dead-time marker and acetonitrile/water 70/30 (v/v) as mobile phase. Figure 4 shows a chromatogram from a microchip with a quadratic 3  $\mu\text{m}$  packing ( $\epsilon_{\text{inter}} = 0.383$ ), acquired at an average flow velocity of  $u = 4.4 \text{ mm s}^{-1}$ , which resulted in a back-pressure of 150 bar. The highly symmetrical peak shapes of the chromatogram in

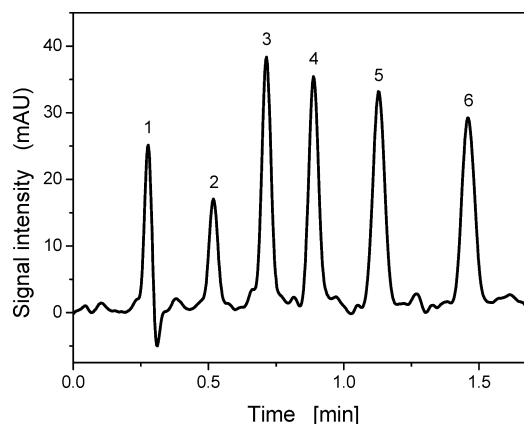


**Figure 4.** Isocratic separation of an alkylbenzene sample (1, uracil; 2, benzene; 3, ethylbenzene; 4, *n*-propylbenzene; 5, *n*-butylbenzene; 6, *n*-pentylbenzene) on a microchip with quadratic separation channel packed with 3  $\mu\text{m}$  porous C8–silica particles: mobile phase, acetonitrile/water 70/30 (v/v) at an average flow velocity of  $u = 4.4 \text{ mm s}^{-1}$ .

Figure 4 were also observed with the other investigated microchip packings. Axial plate heights ( $H$ ) were determined from the *n*-pentylbenzene peak characterized by a retention factor of  $k' = (t_r - t_0)/t_0 = 3.9$  ( $t_r$  is the retention time of *n*-pentylbenzene and  $t_0$  is the dead time of uracil). Figure 5 shows the resulting plate height curves for all investigated microchip packings. Axial plate heights were averaged over two or three individual microchip packings of a given type (conduit geometry, particle size) and thrice-repeated experiments with individual microchips. Good reproducibility was achieved, with ca. 3% variation in plate heights at 1% variation in average flow velocity at the curve minimum. For chromatographic beds of the same packing material and operated with the same mobile phase no differences in the adsorption–desorption kinetics and/or diffusion within the stationary phase are expected. Thus, the observed differences in plate height curves can be ascribed to the respective cross-sectional flow profiles resulting from the actual packing microstructure.

Among the 3  $\mu\text{m}$  packings those with quadratic cross section show the best performance, followed by the trapezoidal packings whose plate height curve is only slightly elevated. Plate height data for quadratic and trapezoidal packings are identical up to an average flow velocity of  $u = 1 \text{ mm s}^{-1}$ , but quadratic packings have the advantage of a relatively small slope at higher velocities. This implies that the analysis time in quadratic packings can be reduced without a significant loss of performance. Gaussian packings display the highest band broaden-

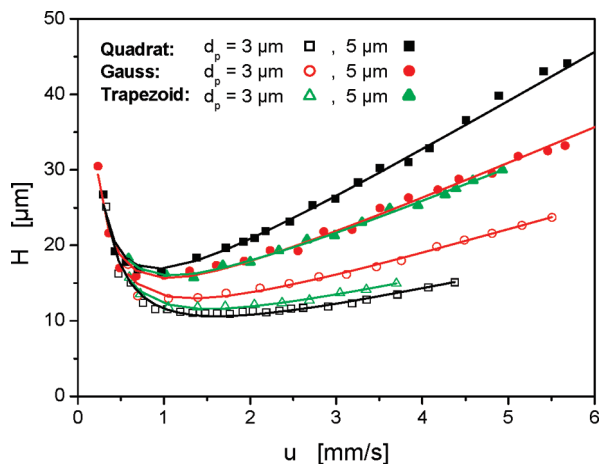


**Figure 5.** Experimental plate height curves for microchips with trapezoidal, quadratic, or Gaussian separation channels packed with 3 or 5  $\mu\text{m}$  porous C8–silica particles: mobile phase, acetonitrile/water 70/30 (v/v); analyte, *n*-pentylbenzene ( $K = 3.9$ ). For each data point the result of three individual chromatographic experiments with a particular microchip packing as well as the results for individual packings of a given type (conduit geometry, particle size) were averaged.

ing, with a higher plate height minimum and steeper slope at higher velocities than the other 3  $\mu\text{m}$  packings. This emphasizes the fact that the conduit geometry significantly influences dispersion even if it does not influence the packing density ( $\epsilon_{\text{inter}} = 0.38$  for all 3  $\mu\text{m}$  packings). For the 3  $\mu\text{m}$  packings, the influence of the conduit geometry on dispersion is comparable with that observed for the empty channels (Figure 3B), i.e., governed by the flow profile as it depends on the conduit cross-sectional geometry and dimensions.

The performance characteristics of the 5  $\mu\text{m}$  packings differ from the corresponding 3  $\mu\text{m}$  packings. Here, the plate height curves of the trapezoidal and Gaussian packings are very similar. Although the Gaussian packings perform slightly better around the minimum, trapezoidal packings gain a small advantage at higher flow velocities. Quadratic packings differ not too much from the other 5  $\mu\text{m}$  packings around the plate height minimum but suffer from a significantly steeper slope at higher velocities. For an explanation of the plate height curves, the different packing densities of the 5  $\mu\text{m}$  packings have to be considered. The higher packing density of the Gaussian 5  $\mu\text{m}$  packings ( $\epsilon_{\text{inter}} = 0.40$ , compared with  $\epsilon_{\text{inter}} = 0.41$  of the trapezoidal 5  $\mu\text{m}$  packings)

partially compensates for the negative influence of the Gaussian profile on dispersion. The sparsely occupied corners of the quadratic channel, which are reflected in the lower density ( $\epsilon_{\text{inter}} = 0.42$ ) of the 5  $\mu\text{m}$  packing, increase the velocity inequality of the macroscopic flow pattern and thus hydrodynamic dispersion.<sup>24</sup> The impact of the lower packing density on band broadening is sufficiently high to overcome the geometrical advantage so that quadratic 5  $\mu\text{m}$  packings demonstrate the worst performance among the investigated microchip packings.

## CONCLUSIONS

Our study has shown that the conduit geometry influences the performance of typical particulate microchip packings in various ways, but the effects cannot be isolated from the particle-aspect ratio of the packings. Although the packing density of the 3  $\mu\text{m}$  packings is not influenced by the conduit geometry, the dispersion behavior reflects dispersion in the empty channels, i.e., is governed by the geometry and dimensions of the conduit cross section. Gaussian 3  $\mu\text{m}$  packings are disadvantaged, whereas the good performance of quadratic 3  $\mu\text{m}$  packings at higher velocities provides an important gain in analysis time.

The dispersion behavior of the 5  $\mu\text{m}$  packings reflects their respective packing densities, which are limited by the number and shape of corners in a channel that determine the inaccessible volume fraction for packing particles. The performance of the Gaussian 5  $\mu\text{m}$  packing is comparable to that of the trapezoidal 5  $\mu\text{m}$  packing, because the higher packing density balances the dispersion disadvantage from the Gaussian conduit shape. On the other hand, quadratic conduits, whose fabrication requires the most effort with the chosen method, lose their symmetry advantage when the particles are difficult to pack densely into the channel.

## ACKNOWLEDGMENT

This work was supported by the Deutsche Forschungsgemeinschaft DFG (Bonn, Germany) under Grant TA 268/4-1 and by an Agilent Technologies Ph.D. Fellowship award through the University Relations Ph.D. Fellowship program.

Received for review September 15, 2009. Accepted November 1, 2009.

AC902069X